Pionless Effective Field Theory Evaluation of Nuclear Polarizability in Muonic Deuterium

Samuel B. Emmons,[1,2] Chen Ji,[3,*] and Lucas Platter[2,4]

[1] *Department of Mathematics, Physics, and Computer Science, Carson-Newman University, Jefferson City, TN 37760, USA*

[2] *Department of Physics and Astronomy, University of Tennessee, Knoxville, TN 37996, USA*

[3] *Key Laboratory of Quark and Lepton Physics, Institute of Particle Physics, Central China Normal University, Wuhan 430079, China*

[4] *Physics Division, Oak Ridge National Laboratory, Oak Ridge, TN 37831, USA*

(Dated: December 3, 2021)

Abstract

We calculate the longitudinal structure function of the deuteron up through next-to-next-to-leading order in the framework of pionless effective field theory. We use these results to compute the two-photon polarizability contribution to Lamb shift in muonic deuterium, which can be utilized to extract the nuclear charge radius of the deuteron. We present analytical expressions order-by-order for the relevant transition matrix elements and the longitudinal structure function, and we give numerical results for the corresponding contributions to the Lamb shift. We also discuss the impact of relativistic and other higher-order effects. We find agreement with previous calculations and explain the accuracy of our calculation.

* jichen@mail.ccnu.edu.cn

I. INTRODUCTION

The deuteron is the simplest bound nuclear system and is made up of only two nucleons. It is the perfect testing ground for new ideas in nuclear theory since calculations are relatively simple for this system and can be compared with decades of experimental data. The electromagnetic properties of a nucleus provide insights into its size, shape, and its continuum properties. These are therefore sensitive observables that test our understanding of short- and long-range charactistics of the nucleon-nucleon interaction.

The charge radius is one of the most elementary electromagnetic observables. It can be measured using either elastic electron-nucleus scattering or laser spectroscopy. An analysis of the world-averaged electron-deuteron scattering data determined the deuteron root-mean-square (rms) charge radius to be $r_d = 2.130(10)$ fm [1]. The transition frequencies among atomic levels in deuterium depend on r_d and an analysis based on the world-averaged deuteron spectroscopy data yields $r_d = 2.1415(45)$ fm [2]. A recent measurement of the Lamb shift in muonic deuterium (μ-d) found a smaller radius, $r_d = 2.12562(78)$ [3], which deviates by 3.5σ from the electronic deuterium (e-d) spectroscopic result. This apparent difference of r_d in e-d and μ-d coincides with the original proton radius puzzle that spurred much theoretical and experimental work after a 7σ deviation was discovered between the proton charge radius extracted from the μ-H Lamb shift, $r_p = 0.84087(39)$ fm [4, 5], and 2016 world-averaged hydrogen spectroscopy data giving $r_p = 0.8759(77)$ fm [6]. Three new spectroscopy experiments have been conducted using electronic hydrogen, two of which [7, 8] agree with the smaller proton radius and one of which [9] agrees with the the larger value. Furthermore, recent electron-proton scattering data from the PRad experiment [10] suggest a smaller proton radius. These new experiments point to a possible resolution of the radius puzzle. However, explanation of discrepancies among different experiments is still needed.

The determination of the nuclear charge radius from μ-d spectroscopy is sensitive to the two-photon exchange (TPE) contribution to the atomic $2S$-$2P$ level spacing [11]. The electromagnetic polarization of the nucleus caused by the muon leads to a distortion of the muon-nucleus wave function and affects thereby the atomic spectrum. In the TPE process, the nucleus is virtually excited and de-excited by the exchange of two photons with the muon. Therefore, TPE depends not only on the bound-state properties of the deuteron, but also on the nucleon-nucleon continuum scattering state and the form of the

electromagnetic current. TPE plays a crucial role in connecting the physics of nuclear structure to photonuclear reactions, and the accuracy of related calculations depends how well known the nuclear Hamiltonian is.

The effects of TPE on μ-d observables were originally calculated in Refs. [12–15] and were recently revisited with improved accuracy using different nuclear models [16–21]. The calculations done with Argonne V18, chiral effective field theory (χEFT), and zero-range approximated (ZRA) nucleon-nucleon interactions show good agreement with each other, demonstrating the high predictive power and accuracy of the state-of-the-art nuclear models. By analyzing statistical and systematic uncertainties on TPE calculations performed within the χEFT framework, the uncertainty due to nuclear model dependence in these calculations was probed [18, 19]. Furthermore, TPE in muonic deuterium was also considered using a dispersion relation analysis of the scattering data [22]. This approach was also shown to agree well with the aforementioned nuclear model calculations. Additional work has extended the evaluation of TPE to other light muonic atoms and ions, *i.e.*, μ^3H, μ^3He$^+$, and μ^4He$^+$ [23–27].

In this work, we make use of the work of Rosenfelder and Leidemann [13, 15] and thereby also more recent calculations that use a state-of-the-art nuclear Hamiltonian [16, 18, 20]. However, instead of χEFT, we will use pionless effective field theory ($\not\pi$EFT). Calculations in this framework can be expanded on an order-by-order basis in an expansion parameter that is proportional to the range of the nuclear interaction R over the two-nucleon scattering length a. The momentum scale of the processes considered within this approach are assumed to be of order $1/a$. $\not\pi$EFT is suited for processes whose momentum scales are well below the pion mass, as in μ-d. For such processes, this approach offers a systematic expansion that is order by order renormalizable, results whose regulator dependence is transparent and understood, and for the two-nucleon systems frequently also analytic results that reveal the dependence on physical parameters directly [28]. Additionally, since the muon is approximately 200 times heavier than the electron, it orbits closer to the nucleus and may be considered as approximately non-relativistic, enabling us to neglect relativistic effects at the EFT order we consider. Compared with χEFT, the order-by-order renormalizability and regulator independence in $\not\pi$EFT provides a rigorous systematic uncertainty estimation which is model-independent. Further, the smaller number of parameters in $\not\pi$EFT make it a powerful tool to explore few-body universality in few-nucleon systems [29].

The organization of this work is as follows. We introduce the basic equations that relate the inelastic structure functions and electric form factors to the TPE effect in muonic deuterium in Sec. II. In Sec. III, we explain the pionless EFT Lagrangian that will be utilized in this work. We then show in Sec. IV how diagrammatic calculations can be used to obtain the inelastic structure function. In Sec. V, we present results for the TPE energy shift obtained from our calculations and compare it to previous calculations. We conclude with a summary and a discussion of possible extensions of this work.

II. THEORY OF TWO-PHOTON EXCHANGE CONTRIBUTIONS

The two-photon exchange contributions in muonic deuterium can be separated into a part depending on the structure of the atomic nucleus and another that depends on the internal dynamics of the single nucleon. In this paper, we focus only on the nuclear two-photon exchange contribution to the former, labeled $\delta^A_{\rm TPE}$, by considering single nucleons as point-like particles. $\delta^A_{\rm TPE}$ consists of the elastic and the inelastic parts

$$\delta^A_{\rm TPE} = \delta^A_{\rm Zem} + \delta^A_{\rm pol} \ , \tag{1}$$

where the elastic part $\delta^A_{\rm Zem}$ corresponds to the nuclear third Zemach moment contribution first derived for light muonic atoms by Friar [30] as a nuclear finite-size contribution of order α^5, where $\alpha = 1/137.036$ denotes the fine structure constant. It is given by [31, 32]

$$\delta^A_{\rm Zem} = -m_r^4 \frac{\alpha^5}{24} \left\langle R^3_{\rm E} \right\rangle_{(2)} = -\, m_r^4 \alpha^5 \frac{2}{\pi} \int_0^\infty \frac{dq}{q^4} \left[F^2_{\rm E}(q^2) - 1 + q^2 \frac{\langle R^2_{\rm E} \rangle}{3} \right] \ , \tag{2}$$

where m_r is the muon-deuteron reduced mass, $F_{\rm E}(q^2)$ is the deuteron electric form factor, and $\langle R^2_{\rm E} \rangle = -6[\partial F_{\rm E}(q^2)/\partial q^2]_{q=0}$, where the derivative is taken with respect to a low-q^2 expansion of $F_{\rm E}(q^2)$.

The inelastic contribution $\delta^A_{\rm pol}$ in Eq. (1) is due to the electric polarization of the nucleus in which the deuteron is virtually excited by exchanging two photons with the muon. This is related to the integral of the forward virtual Compton amplitude that can be written in terms of the nuclear inelastic structure functions [13]. The polarizability term $\delta^A_{\rm pol}$ may be further separated into longitudinal and transverse parts as [13, 15]

$$\delta^A_{\rm pol} = \delta^A_{{\rm pol},L} + \delta^A_{{\rm pol},T} \ , \tag{3}$$

where $\delta^A_{\text{pol},L}$ and $\delta^A_{\text{pol},T}$ are defined respectively as [15]

$$\delta^A_{\text{pol},L} = -8\alpha^2|\phi(0)|^2 \int_0^\infty dq \int_{\omega_{th}}^\infty d\omega K_L(\omega,q) S_L(\omega,q) \ , \tag{4}$$

$$\delta^A_{\text{pol},T} = -8\alpha^2|\phi(0)|^2 \int_0^\infty dq \int_{\omega_{th}}^\infty d\omega \left[K_T(\omega,q) S_T(\omega,q) + K_S(\omega,q) S_T(\omega,0)\right] \ . \tag{5}$$

The variables (ω, q) are the four-momentum carried by the exchanged photon, where $q = |\boldsymbol{q}|$, $\phi(0) = \sqrt{\alpha^3 m_r^3/8\pi}$ is the atomic $2S$-state wave function at origin. To ensure that only the inelastic regime is considered, we have $\omega_{th} \geq B_d + q^2/4m_N$. $B_d = 2.2246$ MeV is the deuteron binding energy, $m_N = 938.92$ MeV is two times the proton-neutron reduced mass, and $q^2/4m_N$ is the recoil energy of the nucleus. S_L and S_T are the longitudinal and transverse deuteron inelastic structure functions, respectively.

The longitudinal integration kernel in Eq. (4) is given by

$$K_L(\omega,q) = \frac{1}{2E_q}\left[\frac{1}{(E_q - m_\mu)(\omega + E_q - m_\mu)} - \frac{1}{(E_q + m_\mu)(\omega + E_q + m_\mu)}\right] \ , \tag{6}$$

where m_μ denotes the muon mass, and $E_q = \sqrt{q^2 + m_\mu^2}$ retains the relativistic kinematics of the muon. The transverse and seagull kernels of Eq. (5) are provided in Ref. [15]. The *seagull* term is required to ensure the gauge invariance and to cancel the infrared singularity near $q = 0$ in the transverse term. In the Coulomb gauge utilized in this paper, the seagull term contributes only to $\delta^A_{\text{pol},T}$ [13]. In the non-relativistic limit $q \ll m_\mu$, the longitudinal kernel in Eq. (6) is approximated in q/m_μ expansion by

$$K_L^{NR} = \frac{1}{q^2(\omega + q^2/2m_\mu)} \ . \tag{7}$$

This kernel's higher-order terms emerge as relativistic corrections.

We note that the expressions for $\delta^A_{\text{pol},L}$ and $\delta^A_{\text{pol},T}$ in Eqs. (4) and (5) were multiplied by an additional factor $R^{(\mu)} = 0.9778$ in Ref. [15] to take into account the modification of muonic deuterium wave function due to the nuclear finite-size correction. However, such a correction is formally an α^6 effect, and is thus neglected in this paper for consistency since the evaluation of δ^A_{pol} and δ^A_{Zem} is of order α^5.

In this work, we compute only relevant contributions up through next-to-next-to-leading order in ∄EFT. Following Rosenfelder [13], we relate the longitudinal part of the structure function S_L to the transition matrix element $\mathcal{M}$ by

$$S_L(\omega, \boldsymbol{q}) = \int \frac{\mathrm{d}^3 p}{(2\pi)^3} \delta(\omega - B_d - \frac{q^2}{4m_N} - \frac{p^2}{m_N}) \, \overline{|\mathcal{M}|^2} \ , \tag{8}$$

where $\overline{|\mathcal{M}|^2}$ is the squared transition matrix element for the electric density operator, between the deuteron ground state and all intermediate excited states.

In the framework of pionless effective field theory ∉EFT, we will calculate the squared matrix element $\overline{|\mathcal{M}|^2}$ relevant to the longitudinal deuteron structure function by considering the coupling of a single A_0 Coulomb photon to the deuteron. We will discuss below that contributions arising from the transverse structure function do not contribute to the order considered here. The deuteron charge form factor $F_E(q^2)$ has been evaluated using ∉EFT in Ref. [33].

III. PIONLESS EFFECTIVE FIELD THEORY

In this section, we provide a brief overview of ∉EFT and the partial-divergence subtraction (PDS) renormalization scheme. We include some details about both the on-shell and off-shell nucleon-nucleon scattering amplitudes that are needed in the transition matrix element calculations required for the structure function calculation of Eq. (8).

A. Lagrangian and Feynman rules

The nucleonic part of the ∉EFT Lagrangian is given by [33]

$$\begin{aligned}\mathcal{L}_0 = N^\dagger\left(i\partial_0 + \frac{\boldsymbol{\nabla}^2}{2m_N}\right)N - C_0\left(N^T P_i N\right)^\dagger\left(N^T P_i N\right)\\ +\frac{C_2}{8}\left[(N^T P_i N)^\dagger\left(N^T P_i \overleftrightarrow{\nabla}^2 N\right) + \text{h.c}\right] - \frac{C_4}{16}\left(N^T P_i \overleftrightarrow{\nabla}^2 N\right)^\dagger\left(N^T P_i \overleftrightarrow{\nabla}^2 N\right) . \quad (9)\end{aligned}$$

where we included the EFT nucleon-nucleon contact interactions in the ${}^3\text{S}_1$-channel up to next-to-next-to-leading order (NNLO) and $P_i = \sigma_2\sigma_i \otimes \tau_2/\sqrt{8}$ is the spin-isospin projection for the ${}^3\text{S}_1$ channel. Additionally, $P_i\overleftrightarrow{\nabla}^2 = P_i\overrightarrow{\partial}^2 + \overleftarrow{\partial}^2 P_i - 2\overleftarrow{\partial}P_i\overrightarrow{\partial}$, and the low-energy constants (LECs) C_i are determined through renormalization by reproducing parameters in the effective range expansion around the deuteron pole. The neutron-proton spin-triplet scattering phase shift is expanded as

$$k\cot\delta_t = -\gamma + \frac{\rho_d}{2}(k^2+\gamma^2) + \cdots , \quad (10)$$

where $\gamma = \sqrt{m_N B_d}$ denotes the deuteron binding momentum and $\rho_d = 1.764$ fm is the effective range. Assuming that the momentum scale of processes considered here is comparable to the deuteron binding momentum, the expansion parameter in ∉EFT is $\gamma\rho_d \approx 0.4$.

We count the nucleon mass as $m_N \approx (\gamma\rho_d)^{-1}\rho_d^{-1}$. Feynman rules corresponding to the Lagrangian given in Eq. (9) give a nucleon propagator as $S(p_0, \boldsymbol{p}) = [p_0 - \boldsymbol{p}^2/2m_N + i\varepsilon]^{-1}$. The first relativistic correction to a two-nucleon matrix element is the kinetic energy multiplied with a term proportional to k^2/m_N^2. Using $k \sim \gamma$ and the aforementioned counting for the nucleon mass we see that this correction enters at $\mathcal{O}\left((\gamma\rho_d)^4\right)$.

Under the $\not\pi$EFT expansion, the LECs are expanded analogously by

$$\begin{aligned} C_0 &= C_{0,-1} + C_{0,0} + C_{0,1} \ , \\ C_2 &= C_{2,-2} + C_{2,-1} \ , \\ C_4 &= C_{4,-3} \ , \end{aligned} \tag{11}$$

where for a coefficient $C_{n,m}$, n denotes the power of momentum in the contact term and $n + m + 1$ indicates the $\not\pi$EFT order at which $C_{n,m}$ emerges. In the power-divergence-subtraction (PDS) scheme, the expanded LECs of Eq. (11) are given by [33, 34]

$$\begin{aligned} C_{0,-1} &= -\frac{4\pi}{m_N}\frac{1}{(\mu-\gamma)} \ , & C_{2,-2} &= \frac{2\pi}{m_N}\frac{\rho_d}{(\mu-\gamma)^2} \ , \\ C_{0,0} &= \frac{2\pi}{m_N}\frac{\rho_d\gamma^2}{(\mu-\gamma)^2} \ , & C_{2,-1} &= -\frac{2\pi}{m_N}\frac{\rho_d^2\gamma^2}{(\mu-\gamma)^3} \ , \\ C_{0,1} &= -\frac{\pi}{m_N}\frac{\rho_d^2\gamma^4}{(\mu-\gamma)^3} \ , & C_{4,-3} &= -\frac{\pi}{m_N}\frac{\rho_d^2}{(\mu-\gamma)^3} \ , \end{aligned} \tag{12}$$

where μ is the PDS renormalization scale.

The electromagnetic interaction with the nucleon field is included by replacing the four-gradient with the minimally-coupled gauge covariant derivative $D_\mu = \partial_\mu + ie\mathcal{Q}A_\mu$, where $\mathcal{Q} = (1+\tau_3)/2$ denotes the nucleon charge operator with Pauli matrix τ_3 acting in isospin space and A_μ is the electromagnetic gauge field. The Lagrangian for the induced electromagnetic interaction is thus given by

$$\mathcal{L}_{\rm EM} = -eN^\dagger\mathcal{Q}NA_0 + \frac{ie}{2m_N}\left[N^\dagger\mathcal{Q}(-\overleftarrow{\nabla} + \overrightarrow{\nabla})N\right]\cdot\boldsymbol{A} - \frac{e^2}{2m_N}N^\dagger Q\boldsymbol{A}\cdot\boldsymbol{A}QN \, , \tag{13}$$

where the last term is a two-photon coupling and yields the seagull term in the two-photon exchange, which contributes only to $\delta_{{\rm pol},T}$ when Coulomb gauge is adopted [13]. We also drop the two-nucleon current from the minimal coupling within the contact interactions, because it only enters at higher orders than the NNLO considered in this paper.

The nucleon current from one-photon coupling is given by

$$J^\mu(\boldsymbol{p}, \boldsymbol{p}') = e\mathcal{Q}\left(1, \frac{\boldsymbol{p}+\boldsymbol{p}'}{2m_N}\right) . \tag{14}$$

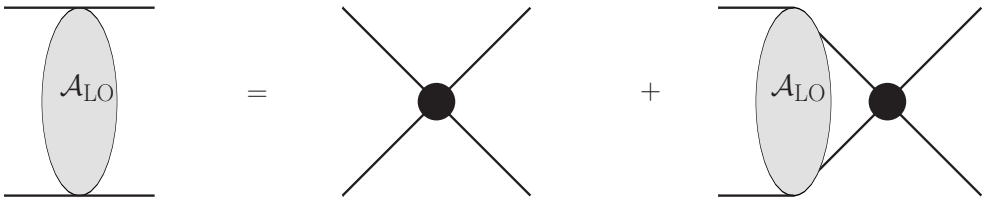

FIG. 1. Diagrammatic representation of the Lippmann-Schwinger equation for the LO two-body scattering amplitude $\mathcal{A}_{\rm LO}$. The round vertex represents insertion of the LO contact term.

We see that the transverse current enters the transition matrix element with a factor of k/m_N. This implies that the squared matrix element entering the calculation of the transverse structure factor is also $\mathcal{O}((\gamma\rho_d)^4)$.

B. Leading order nucleon-nucleon amplitude

We denote the leading order amplitude in the triplet channel as $\mathcal{A}_{\rm LO}$, which is shown diagrammatically in Fig. 1. This is the Lippmann-Schwinger equation and is solved by identifying the expression in the figure as the iterative sum

$$i\mathcal{A}_{\rm LO}(E) = -iC_{0,-1}\left[1 - \mathcal{I}_0(E)\mathcal{A}_{\rm LO}(E)\right] \ , \tag{15}$$

where E is the two-nucleon energy in the center of mass frame and $\mathcal{I}_0$ indicates the loop integral defined in Eq. (A1). $\mathcal{I}_0$ is solved using the PDS scheme [34] and its dependence on the renormalization scale μ is given in Eq. (A1). The leading-order amplitude

$$\mathcal{A}_{\rm LO}(E) = -\frac{4\pi}{m_N}\frac{1}{\gamma + ip} \ , \tag{16}$$

is obtained using Eq. (15) and taking the expression of $C_{0,-1}$ in Eq. (12), where $p = \sqrt{m_N E}$ is the nucleon-nucleon on-shell relative momentum.

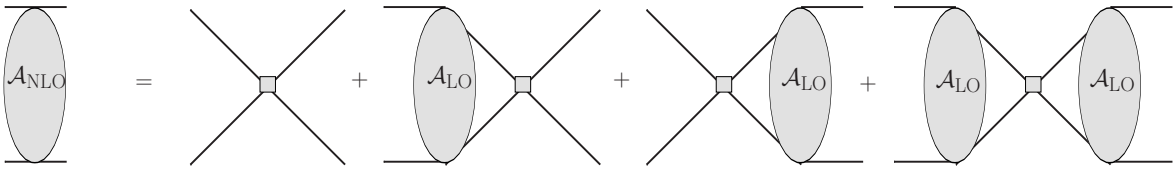

FIG. 2. Diagrammatic representation of the NLO amplitude calculated perturbatively. The square vertex indicates the insertion of an NLO vertex rule.

C. Next-to-leading order amplitude

The diagrams required to evaluate the next-to-leading-order (NLO) are shown in Fig. 2 and lead to the NLO half-off-shell amplitude

$$\begin{aligned} i\mathcal{A}_{\rm NLO}(k,p;E) =& -iC_{0,0}\left[1+i\mathcal{I}_0 i\mathcal{A}_{\rm LO}\right]^2 - iC_{2,-2}(1+i\mathcal{I}_0 i\mathcal{A}_{\rm LO})\left[\frac{k^2+p^2}{2}+i\mathcal{I}_2 i\mathcal{A}_{\rm LO}\right] \\ =& -i\frac{2\pi}{m_N}\frac{\rho_d}{\gamma+ip}\left[\gamma-ip+\frac{1}{2(\gamma-\mu)}\left(k^2-p^2\right)\right] . \end{aligned} \tag{17}$$

where the loop integrals $\mathcal{I}_0$, $\mathcal{I}_2$ and the amplitude $\mathcal{A}_{\rm LO}$ are evaluated at the center-of-mass energy $E = p^2/m_N$, and k is the incoming-state momentum. We arrive at the second line of Eq. (17) using the Lippmann-Schwinger equation (15) and using $\mathcal{I}_{2n} = p^{2n}\mathcal{I}_0$ from Eq. (A1). On the energy shell, the incoming momentum equals the on-shell momenta $k = p$. This yields the on-shell NLO amplitude

$$\mathcal{A}_{\rm NLO}(p,p,E) = -\frac{2\pi\rho_d}{m_N}\frac{\gamma-ip}{\gamma+ip} . \tag{18}$$

D. Next-to-next-to-leading order amplitude

To obtain the NNLO amplitude, we make use of a diagrammatic expression including all NNLO diagrams. After replacing the couplings in the resulting expression using Eq. (12), we find the half-off-shell NNLO amplitude to be

$$\mathcal{A}_{\rm NNLO}(k,p;E) = -\frac{\pi}{m_N}\frac{\rho_d^2}{\gamma+ip}\left[(\gamma-ip)^2+\frac{\gamma-ip}{\gamma-\mu}\left(1+\frac{\gamma+ip}{\gamma-\mu}\right)\frac{k^2-p^2}{2}\right] . \tag{19}$$

The NNLO on-shell amplitude is found after setting $k = p$ and is

$$\mathcal{A}_{\rm NNLO}(p,p,E) = -\frac{\pi\rho_d^2}{m_N}\frac{(\gamma-ip)^2}{\gamma+ip} . \tag{20}$$

The μ-dependence of Eq. (19) is removed in the on-shell amplitude of Eq. (20).

E. Deuteron electric form factor

In the vicinity of the bound-state pole $p = i\gamma$, the on-shell amplitude is given by

$$\mathcal{A}_d(E) = -\frac{\mathcal{Z}_d}{E + \gamma^2/m_N} \ , \tag{21}$$

where $\mathcal{Z}_d$ is the wave function renormalization factor related to ρ_d and γ as

$$\mathcal{Z}_d = \frac{8\pi\gamma}{m_N^2(1 - \rho_d\gamma)} \ . \tag{22}$$

Eqs. (21) and (22) are needed in the calculation of the deuteron electric form factor that has been calculated up to NNLO in ∉EFT as [33]

$$F_{\rm E}(q^2) = \frac{1}{1 - \rho_d\gamma}\left[\frac{4\gamma}{q}\arctan\frac{q}{4\gamma} - \rho_d\gamma\right] \ . \tag{23}$$

The form factor of Eq. (23) is needed in evaluating the third Zemach moment contribution to the Lamb Shift in muonic deuterium given by Eq. (2).

IV. DIAGRAMMATIC CALCULATION OF TRANSITION MATRIX ELEMENTS

In this section, we use ∉EFT Feynman diagrams to evaluate the longitudinal transition matrix elements up to its NNLO contribution, which is needed for the evaluation of the longitudinal structure function and the polarizability effect.

A. Transition matrix element at LO

At LO, the transition matrix element from the A_0-photon excitation of the deuteron is depicted by the Feynman diagrams in Fig. 3. The first two diagrams, (a) and (b), are contributions without final state interactions, while the third diagram contains final state interactions as indicated by a shaded grey oval symbolizing an insertion of the LO scattering amplitude. Figure 3 also displays the kinematics we use in the calculation of this matrix element. Note that the incoming deuteron is at rest, so the total energy of the initial two-nucleon state is therefore $-B_d$. The final two-nucleon state has energy $E = p^2/m_N$.

We evaluate the plane-wave contribution by calculating the amplitude without projecting on specific spin-orbit coupled final states and are thereby summing up all electric multipoles contributing to the transition induced by the A_0 photon. The plane-wave final states are

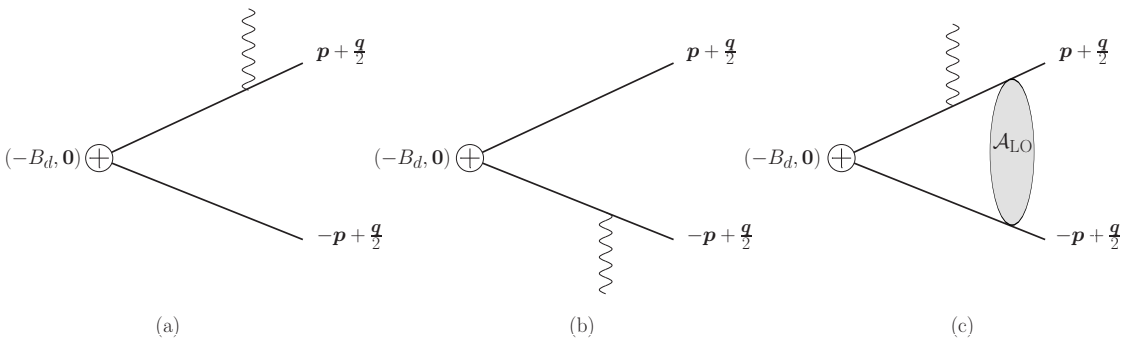

FIG. 3. Contribution to the leading order transition matrix element needed for the inelastic longitudinal structure function. The wavy line denotes the coupling of the electromagnetic current to the nucleon.

represented by two nucleon spinors N^T and N for each outgoing nucleon leg. N holds a tensor product of the two-component spinor for spin and the two-component spinor for isospin. The initial deuteron ${}^3\mathrm{S}_1$ state is projected out by the operator P_i. The antisymmetrization is treated by including both diagrams where the photon either couples to the top or the bottom leg as shown in diagrams (a) and (b) of Fig. 3.

For diagram (a) in Fig. 3, we obtain

$$\begin{aligned}(i\mathcal{M}^a_{\rm LO})^i_{\alpha\beta} &= i2\sqrt{\mathcal{Z}_d} iS(-B_d - \tfrac{(-\boldsymbol{p}+\boldsymbol{q}/2)^2}{2m_N}, \boldsymbol{p} - \tfrac{\boldsymbol{q}}{2})\, N^T_\alpha(\boldsymbol{p}+\frac{\boldsymbol{q}}{2})\mathcal{Q}P_i^\dagger N_\beta(-\boldsymbol{p}+\frac{\boldsymbol{q}}{2}) \\ &= i\sqrt{\mathcal{Z}_d} i\tilde{M}^a_{\rm LO} N^T_\alpha(\mathbf{p}+\frac{\boldsymbol{q}}{2})\mathcal{Q}P_i^\dagger N_\beta(-\boldsymbol{p}+\frac{\boldsymbol{q}}{2}). \end{aligned} \tag{24}$$

where we defined the amplitude $\tilde{M}^a_{\rm LO} = -2m_N/\left[\gamma^2 + (\boldsymbol{p}-\boldsymbol{q}/2)^2\right]$. The indices α and β on the nucleon spinors denote spin and isospin basis indices, and i is the deuteron spin index. Note that a factor of 2 is included in Eq. (24) to account for both possible contractions leading to that expression. Similarly, diagram (b) in Fig. 3 yields

$$(i\mathcal{M}^b_{\rm LO})^i_{\alpha\beta} = i\sqrt{\mathcal{Z}_d} i\tilde{M}^b_{\rm LO} N^T_\alpha(\mathbf{p}+\frac{\boldsymbol{q}}{2}) P_i^\dagger \mathcal{Q} N_\beta(-\boldsymbol{p}+\frac{\boldsymbol{q}}{2})\,, \tag{25}$$

where the amplitude $\tilde{M}^b_{\rm LO} = -2m_N/\left[\gamma^2 + (\boldsymbol{p}+\boldsymbol{q}/2)^2\right]$.

Furthermore, we evaluate the contributions with ${}^3\mathrm{S}_1$ final-state interactions at LO, using the diagram (c) shown in Fig. 3. The excitation from ${}^3\mathrm{S}_1$ bound state to the ${}^1\mathrm{S}_0$ scattering state is forbidden by the A_0 photon. The iterative sum of final-state interactions is represented by the off-shell scattering amplitude $P_i^\dagger i\mathcal{A}_{\rm LO} P_i$.

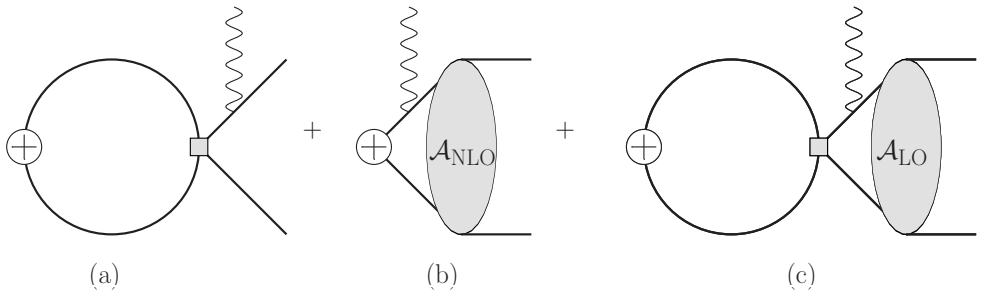

FIG. 4. NLO diagrammatic contribution to the matrix element $\mathcal{M}$. Final state S-wave interactions are indicated by the grey blob. We have omitted one diagram without final state interactions where the photon couples to the lower outgoing leg.

Using the Feynman rules we obtain for this diagram the transition matrix element

$$(i\mathcal{M}^c_{\rm LO})^i_{\alpha\beta} = i8\sqrt{\mathcal{Z}_d}\,{\rm Tr}\left[P_i^\dagger \mathcal{Q} P_j\right] i\mathcal{A}_{\rm LO}(E)\, N^T_\alpha(\boldsymbol{p}+\frac{\boldsymbol{q}}{2}) P_j^\dagger N_\beta(-\boldsymbol{p}+\frac{\boldsymbol{q}}{2}) \\ \times \int \frac{{\rm d}^4 l}{(2\pi)^4} iS(-B_d+l_0, \boldsymbol{l}-\frac{\boldsymbol{q}}{2}) iS(-B_d+l_0+\omega, \boldsymbol{l}+\frac{\boldsymbol{q}}{2}) iS(-l_0, \boldsymbol{l}-\frac{\boldsymbol{q}}{2})\ . \quad (26)$$

Note that a factor of 8 is included for the possible number of contractions in the matrix element evaluation. The loop integral arising in the calculation of diagram (c) in Fig. 3 we label as $\mathcal{J}_0$, and after evaluating the trace ${\rm Tr}[P_i^\dagger \mathcal{Q} P_j] = \delta_{ij}/4$ in Eq. (26), we find

$$(i\mathcal{M}^c_{\rm LO})^i_{\alpha\beta} = i\sqrt{\mathcal{Z}_d} i\tilde{M}^c_{\rm LO} N^T_\alpha(-\boldsymbol{p}+\frac{\boldsymbol{q}}{2}) P_i^\dagger N_\beta(\boldsymbol{p}+\frac{\boldsymbol{q}}{2})\ , \quad (27)$$

where $\tilde{M}^c_{\rm LO} = 2\mathcal{J}_0\mathcal{A}_{\rm LO}(E)$. The definition and the derivation of the $\mathcal{J}_0$ integral result are given in App. A 2.

Below, at NLO and NNLO, we will use the short-hand notation introduced above and work with the amplitudes $\tilde{M}$ with $\sqrt{Z_d}$ and the spinor pieces factored out. Amplitudes with superscripts a or b will continue to correspond to diagrams without final-state interactions, while those with superscript c correspond to diagrams at a given order that contain final-state interactions.

B. Transition matrix element at NLO

Diagrams that contribute to the transition matrix element at NLO are shown in Fig. 4. The diagram with one NLO contact that has no final state interactions is given by diagram

(a) of Fig. 4. After antisymmetrization, it leads to the expressions

$$\begin{aligned} i\tilde{M}^{a}_{\rm NLO} =& 2\left[(-i\frac{C_{2,-2}}{2})\left(i\mathcal{I}_0(-B_d)\left(\boldsymbol{p}-\tfrac{\boldsymbol{q}}{2}\right)^2+i\mathcal{I}_2(-B_d)\right)+(-iC_{0,0})i\mathcal{I}_0(-B_d)\right] \\ & \times iS(-B_d-\tfrac{(-\boldsymbol{p}+\boldsymbol{q}/2)^2}{2m_N},\boldsymbol{p}-\tfrac{\boldsymbol{q}}{2}) \\ =& i\frac{\rho_d}{2}m_N(\mu-\gamma)^{-1} \end{aligned} \tag{28}$$

and

$$i\tilde{M}^{b}_{\rm NLO} = i\frac{\rho_d}{2}m_N(\mu-\gamma)^{-1}\ , \tag{29}$$

where we used that $-\mathcal{I}_2(-B_d)=\gamma^2\mathcal{I}_0(-B_d)$ and $C_{0,0}=\gamma^2 C_{2,-2}$.

Diagram (b) of Fig. 4 gives the contribution with no explicit contact term insertion, but with one NLO final-state scattering amplitude.[1] It leads to

$$\begin{aligned} i\tilde{M}^{c,0}_{\rm NLO} =& 2\frac{\rho_d}{2}i\mathcal{A}_{\rm LO}(E)\int\frac{{\rm d}^3k}{(2\pi)^3}iS(-B_d-\frac{k^2}{2m_N},\boldsymbol{k})iS(-B_d+\omega-\frac{k^2}{2m_N},\boldsymbol{k}+\boldsymbol{q}) \\ & \times\left[(\gamma-ip)+\frac{1}{2(\gamma-\mu)}(v^2-p^2)\right], \end{aligned} \tag{30}$$

where $v=|\mathbf{k}+\frac{\mathbf{q}}{2}|$ and the half off-shell NLO amplitude $\mathcal{A}_{\rm NLO}(v,p,E)$ of Eq. (17) depending on the loop momentum k was inserted. Using the definitions from the appendix for the loops that couple to the photon, we can write

$$\begin{aligned} i\tilde{M}^{c,0}_{\rm NLO} &= 2i\mathcal{A}_{\rm LO}(E)\frac{\rho_d}{2}\left[(\gamma-ip)\mathcal{J}_0+\frac{1}{2(\gamma-\mu)}\left(\tilde{\mathcal{J}}_2-p^2\mathcal{J}_0\right)\right] \\ &= \frac{\rho_d}{2}i\mathcal{A}_{\rm LO}(E)\left[2(\gamma-ip)\mathcal{J}_0+\frac{m_N^2}{4\pi}\right], \end{aligned} \tag{31}$$

where $\tilde{\mathcal{J}}_2$ is defined in Eq. (A8) and we used the result of Eq. (A10) in App. A 3 to replace $\left(\tilde{\mathcal{J}}_2-p^2\mathcal{J}_0\right)$. Diagram (c) of Fig. 4 with one NLO operator and one LO scattering amplitude yields an amplitude we label $i\tilde{M}^{c,1}_{\rm NLO}$. Combining the sum of loop integrals and using the identities $C_{0,0}=\gamma^2C_{2,-2}$ and $\mathcal{I}_2(-B_d)=-\gamma^2\mathcal{I}_0(-B_d)$ allows for this amplitude to be written

$$\begin{aligned} \tilde{M}^{c,1}_{\rm NLO} &= C_{2,-2}\mathcal{I}_0(-B_d)(\mathcal{J}_2+\gamma^2\mathcal{J}_0)\mathcal{A}_{\rm LO}(E) \\ &= -\frac{\rho_d}{2}\frac{m_N}{\mu-\gamma}\mathcal{I}_0(E)\mathcal{A}_{\rm LO}(E)\ , \end{aligned} \tag{32}$$

[1] The diagram label (b) in Fig. 4 is not connected with the superscript c indicating final-state interactions.

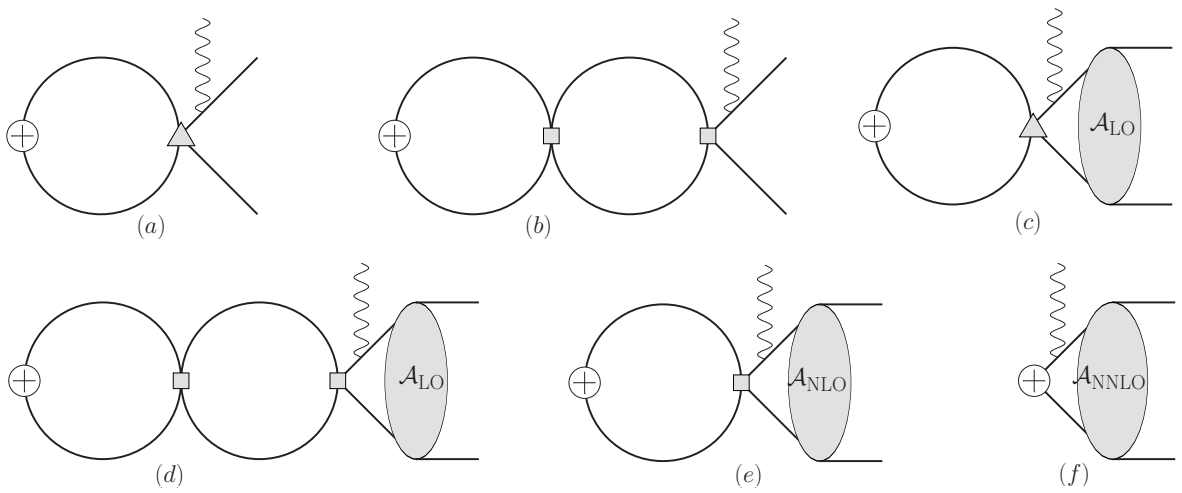

FIG. 5. NNLO diagrammatic contribution to the matrix element $\mathcal{M}$ that includes one insertion of NNLO operator or two insertions of NLO operator. The grey square and triangle denote the collection of NLO and NNLO operators, respectively. These diagrams make zero contributions after renormalization.

where the expressions for loop integrals from Eq. (A7) are used. The summation of Eqs. (31) and (32) yields

$$\begin{aligned}\tilde{M}^{c}_{\rm NLO} =& \tilde{M}^{c,0}_{\rm NLO} + \tilde{M}^{c,1}_{\rm NLO} \ , \\ =& \frac{\rho_d}{2}\mathcal{A}_{\rm LO}(E)\left[2(\gamma - ip)\mathcal{J}_0 + \frac{m_N^2}{4\pi}\left(1 + \frac{\mu + ip}{\mu - \gamma}\right)\right] \ . \end{aligned} \tag{33}$$

C. Transition matrix element at NNLO

In Fig. 5, we show the diagrams contributing at NNLO. Diagrams (a) and (b) in Fig. 5 generate the NNLO contributions to $\mathcal{M}^a$ and $\mathcal{M}^b$. The sum of these diagrams give no contribution because $\tilde{M}^{a}_{\rm NNLO} = \tilde{M}^{b}_{\rm NNLO} = 0$. Diagrams (c) and (d) in Fig. 5 evaluate to zero, too. Diagrams (e) and (f) in Fig. 5 represent the non-zero contributions to the transition matrix element at NNLO. Diagram (e) gives the contributions with one insertion of one NLO operator and one NLO amplitude. Its contribution to $\mathcal{M}^c$ yields

$$\begin{aligned} i\tilde{M}^{c,0}_{\rm NNLO} &= C_{2,-2}\mathcal{I}_0(-B_d)(\mathcal{J}_2 + \gamma^2\mathcal{J}_0)\frac{\rho_d}{2}i\mathcal{A}_{\rm LO}(E)(\gamma - ip) \ , \\ &= i\mathcal{A}_{\rm LO}(E)\left(\frac{\rho_d}{2}\right)^2\frac{m_N^2}{4\pi}(\gamma - ip)\frac{\mu + ip}{\mu - \gamma} \ , \end{aligned} \tag{34}$$

where the expression of loop integral in Eq. (A7) is used. Inserting the half-off-shell NNLO amplitude in diagram (f), we obtain

$$\begin{aligned} i\tilde{M}^{c,1}_{\rm NNLO} &= 2i\mathcal{A}_{\rm LO}(E)\left(\frac{\rho_d}{2}\right)^2\left[(\gamma-ip)^2\mathcal{J}_0+\frac{\gamma-ip}{2(\gamma-\mu)}(\tilde{\mathcal{J}}_2-p^2\mathcal{J}_0)(1+\frac{\gamma+ip}{\gamma-\mu})\right] \\ &= 2i\mathcal{A}_{\rm LO}(E)\left(\frac{\rho_d}{2}\right)^2\left[(\gamma-ip)^2\mathcal{J}_0+\frac{m_N^2}{8\pi}(\gamma-ip)(1+\frac{\gamma+ip}{\gamma-\mu})\right] . \end{aligned} \tag{35}$$

The regulator-dependence in the NNLO contribution is removed when Eqs. (34) and (35) are summed together as

$$\tilde{M}^{c}_{\rm NNLO} = 2\mathcal{A}_{\rm LO}(E)\left(\frac{\rho_d}{2}\right)^2(\gamma-ip)\left[(\gamma-ip)\mathcal{J}_0+\frac{m_N^2}{4\pi}\right] . \tag{36}$$

We note that the S-D wave mixing operator enters at NNLO in the ≠EFT Lagrangian, and in principle gives a contribution to the transition matrix element at the same order. However, due to the orthogonality of S-wave and D-wave component, contributions from the D-wave projection to the squared matrix element does not interfere with the S-wave projection. Therefore, the S-D mixing contributions enter at N4LO in the squared matrix element, and we therefore do not consider this higher-order effect.

D. Matrix element squared

The calculation of the inelastic longitudinal structure function in Eq. (8) requires the squared matrix elements and a sum over the outgoing nucleon-nucleon spin and isospin states. This sum leads to traces of products of projection and charge operators. We carry this out without projecting the outgoing state on a specific spin or isospin coupling. We write

$$\overline{|\mathcal{M}|^2} = \frac{1}{2}\sum_{\alpha\beta}|\mathcal{M}^a_{\alpha\beta}+\mathcal{M}^b_{\alpha\beta}+\mathcal{M}^c_{\alpha\beta}|^2 , \tag{37}$$

where the factor of 1/2 is introduced to account for the identicality of particles in the intermediate state. The summation over outgoing spins converts the included spin-projected matrix elements into traces over the corresponding projectors. After evaluating the traces arising in Eq. (37), we obtain

$$\overline{|\mathcal{M}|^2} = \frac{\mathcal{Z}_d}{4}\left(\left|\frac{\tilde{M}^a-\tilde{M}^b}{2}\right|^2+\left|\frac{\tilde{M}^a+\tilde{M}^b}{2}+\tilde{M}^c\right|^2\right) , \tag{38}$$

where the amplitudes on the right hand side can be expanded order-by-order. The first term in Eq. (38) receives no NLO or NNLO corrections since $\tilde{M}^a_{\rm NLO} - \tilde{M}^b_{\rm NLO} = 0$, as can be seen from Eqs.(28) and (29), and $\tilde{M}^a_{\rm NNLO} = \tilde{M}^b_{\rm NNLO} = 0$.

The second term in Eq. (38) receives LO, NLO, and NNLO contributions, but the NNLO contribution arises only from $\tilde{M}^c_{\rm NNLO}$, given in Eq. (36). We can therefore write the squared amplitude up through NNLO as

$$\begin{aligned}\overline{|\mathcal{M}|^2} =& \frac{\mathcal{Z}_d}{4}\Bigg\{\left|\frac{\tilde{M}^a_{\rm LO} - \tilde{M}^b_{\rm LO}}{2}\right|^2 + \left|\frac{\tilde{M}^a_{\rm LO} + \tilde{M}^b_{\rm LO}}{2}\right. \\ &\left. + 2\mathcal{A}_{\rm LO}(E)\left[\mathcal{J}_0\left(\sum_{n=0}^{2}\left(\frac{\rho_d}{2}\right)^n(\gamma - ip)^n\right) + \frac{\rho_d}{2}\frac{m_N^2}{4\pi}\left(1 + \frac{\rho_d}{2}(\gamma - ip)\right)\right]\right|^2\Bigg\}\,. \end{aligned} \tag{39}$$

V. RESULTS

Analytical results for the inelastic longitudinal structure function can be calculated by inserting Eq. (39) into the integrand in Eq. (8). Once the structure function is obtained at each order we consider in this work, we compute $\delta^A_{{\rm pol},L}$ order-by-order. We extract the electric dipole contribution for comparison with other works that carry out an explicit multipole decomposition [15, 20]. Additionally, we calculate the third inelastic Zemach moment term $\delta^A_{\rm Zem}$.

A. Results for the longitudinal structure function

To demonstrate the order-by-order convergence of the $\not\pi$EFT calculation of the longitudinal structure function S_L, we extract the $\rho_d\gamma$ power dependence at each order. Besides the explicit $\rho_d\gamma$ dependence in Eq. (39), we expand the the deuteron renormalization constant $\mathcal{Z}_d$ in powers of $\rho_d\gamma$ as

$$\mathcal{Z}_d = \frac{8\pi\gamma}{m_N^2}\left(1 + \rho_d\gamma + \rho_d^2\gamma^2 + \cdots\right), \tag{40}$$

to include the order-by-order correction from the wave function renormalization.

At leading order we find the inelastic structure function result

$$\begin{aligned} S_L^{\rm LO}(q,\omega) =& \frac{\gamma p}{\pi m_N}\left[\frac{2m_N^2}{m_N^2\omega^2 - q^2p^2} + \frac{32\pi^2}{m_N^2(\gamma^2+p^2)}\right. \\ &\left.\times\left(\left({\rm Re}\big[\mathcal{J}_0\big]\right)^2 - \frac{2\gamma}{p}{\rm Re}\big[\mathcal{J}_0\big]{\rm Im}\big[\mathcal{J}_0\big] - \left({\rm Im}\big[\mathcal{J}_0\big]\right)^2\right)\right], \end{aligned} \tag{41}$$

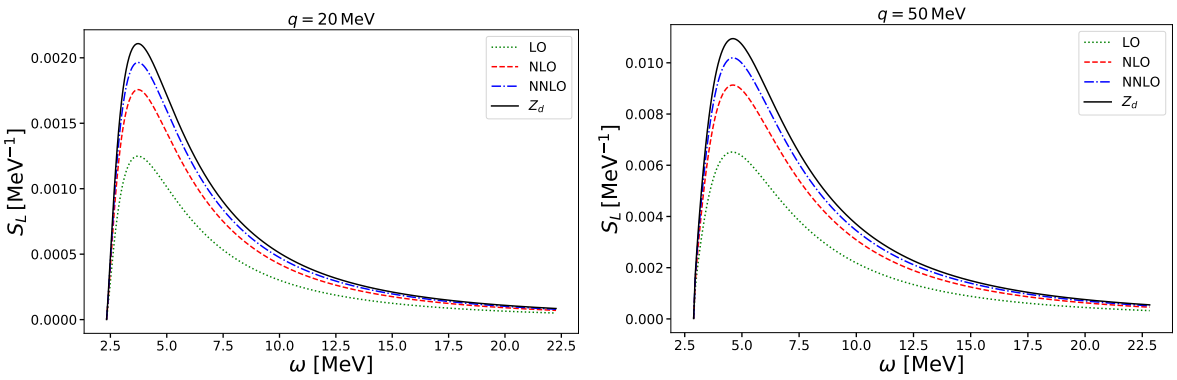

FIG. 6. Longitudinal structure function S_L as a function of ω at fixed momentum exchange $q = 20$ MeV (left panel) and $q = 50$ MeV (right panel). The dotted, dashed, dot-dashed lines give the result of the LO, NLO and NNLO structure function, respectively. The solid line gives NNLO $\mathcal{Z}_d$-improved result.

where $p = \sqrt{m_N\omega - \gamma^2 - q^2/4}$. At NLO, the inelastic longitudinal structure function we calculate as

$$S_L^{\rm NLO}(q,\omega) = \rho_d\gamma S_L^{\rm LO}(q,\omega) + \frac{8\rho_d\gamma}{m_N(\gamma^2+p^2)}\Bigg\{p{\rm Re}\left[\mathcal{J}_0\right] - \gamma{\rm Im}\left[\mathcal{J}_0\right] + \frac{4\pi}{m_N^2}\Big[\gamma p\left(({\rm Re}\left[\mathcal{J}_0\right])^2 - ({\rm Im}\left[\mathcal{J}_0\right])^2\right) + (p^2-\gamma^2){\rm Re}\left[\mathcal{J}_0\right]{\rm Im}\left[\mathcal{J}_0\right]\Big]\Bigg\}. \quad (42)$$

Lastly, the N2LO part of the inelastic structure function is

$$S_L^{\rm NNLO} = \rho_d\gamma S_L^{\rm NLO}(q,\omega) + \frac{m_N\gamma\rho_d^2}{2\pi(\gamma^2+p^2)}\Bigg\{p + \frac{8\pi}{m_N^2}\Big[2\gamma p{\rm Re}\left[\mathcal{J}_0\right] + (p^2-\gamma^2){\rm Im}\left[\mathcal{J}_0\right]\Big] + \frac{16\pi^2}{m_N^4}\Big[(p^3-3p\gamma^2)\left({\rm Im}\left[\mathcal{J}_0\right]^2 - {\rm Re}\left[\mathcal{J}_0\right]^2\right) + (6p^2\gamma - 2\gamma^3){\rm Re}\left[\mathcal{J}_0\right]{\rm Im}\left[\mathcal{J}_0\right]\Big]\Bigg\}. \quad (43)$$

The EFT convergence of the structure function is shown in Fig. 6, where $S_L(\omega, q)$ is plotted as a function of ω by fixing q at 20 MeV and 50 MeV in the two different plots in the figure. Calculations of $S_L(\omega, q)$ at LO, NLO, and NNLO are compared in the plots, which show an order-by-order convergence in $\not\pi$EFT.

B. Benchmark with dipole approximation results

As mentioned previously, we do not perform our calculation using a multipole decomposition as in Refs. [15, 20]. Instead, the integration to determine $\delta^A_{{\rm pol},L}$ in Eq. (4) was taken using

the complete inelastic longitudinal structure function of the nucleus, given order-by-order in Eqs. (41), (42), and (43), that implicitly contains all inelastic multipole contributions. However, we extract the inelastic dipole excitation for comparison with previous literature. This is motivated by the fact that the dipole excitation gives the largest contribution to TPE.

The electric-dipole excitation of the nucleus arises when the outgoing unbound nucleons are in a spin-singlet isospin-triplet state. The antisymmetry of the wave function is preserved by the fact that the outgoing NN state has odd orbital angular momentum. The first term in the low-momentum approximation of the squared matrix element in Eq. (38) corresponds to a P wave between the outgoing nucleons and is

$$\overline{|\mathcal{M}|^2} \approx \frac{\mathcal{Z}_d}{4}\left|\frac{\tilde{M}^a_{\rm LO}-\tilde{M}^b_{\rm LO}}{2}\right|^2 \approx m_N^2\mathcal{Z}_d\frac{(\boldsymbol{p}\cdot\boldsymbol{q})^2}{(\gamma^2+p^2)^4}\ . \tag{44}$$

Inserting the matrix element $\overline{|\mathcal{M}|^2}$ into a low-q truncated version of Eq. (8) by dropping the recoil energy $q^2/4m_N$ gives the dipole part of the inelastic longitudinal structure function as

$$\begin{aligned} S_D(|\boldsymbol{q}|,\omega) =& \int\frac{\mathrm{d}^3p}{(2\pi)^3}\delta(\omega-\frac{\gamma^2}{m_N}-\frac{p^2}{m_N})\,\overline{|\mathcal{M}|^2} \\ =& \frac{\mathcal{Z}_d\sqrt{m_N}}{12\pi^2}\frac{(\omega-\gamma^2/m_N)^{3/2}}{\omega^4}q^2\,. \end{aligned} \tag{45}$$

Plugging the dipole structure function $S_D(|\boldsymbol{q}|,\omega)$ of Eq. (45) and the non-relativistic kernel K_L^{NR} from Eq. (7) into the TPE energy-shift equation given by Eq. (4) yields

$$\delta^A_{\mathrm{pol},D} = -\frac{4\pi}{3}\alpha^2\phi^2(0)\frac{\mathcal{Z}_d m_N^{5/2}\sqrt{2m_r}}{35\pi^2\gamma^4}\ , \tag{46}$$

which matches the expression of the same contribution in Ref. [21]. In the above expression, we replaced m_μ with the μ-d reduced mass m_r to adjust the truncation of recoil correction in the low-q approximation. The numerical evaluation of the dipole term given by Eq. (46) yields $\delta^A_{\mathrm{pol},D} = -1.925$ meV.

C. Numerical results for TPE contribution to Lamb shift

The TPE contribution to the Lamb shift in muonic deuterium can be calculated order-by-order in ∉EFT to the desired precision. We do so up to NNLO in an expansion in the parameter $\rho_d\gamma$. To evaluate the elastic TPE, Zemach term δ^A_{Zem}, we insert the electric form

$\delta^A_{\mathrm{pol},L}$	NR limit	R limit
$\not\pi$EFT LO	-0.962	-0.943
$\not\pi$EFT NLO	-1.346	-1.320
$\not\pi$EFT NNLO	-1.499	-1.470
$\mathcal{Z}_d$ improved	-1.605	-1.574
dipole term	-1.925	–
ZRA (η-less)	-1.590	-1.553
ZRA (η-expansion)	-1.590	-1.564
χEFT (η-less)	-1.588	-1.562
χEFT (η-expansion)	-1.590	-1.560

TABLE I. The longitudinal polarizability $\delta^A_{\mathrm{pol},L}$ is calculated in both non-relativistic and relativistic limit. Results in $\not\pi$EFT are calculated in this work at LO, NLO, NNLO and with the NNLO $\mathcal{Z}_d$-improvement approach. Results from other works in dipole approximation, ZRA and χEFT are extracted from information in Refs. [20, 21, 27].

factor F_{E} from Eq. (23) into the integral equation (2). δ^A_{Zem} is evaluated to be $-0.362\,\mathrm{meV}$, which is consistent with the calculation in Ref. [20].

The longitudinal polarizability $\delta^A_{\mathrm{pol},L}$ is firstly evaluated in the non-relativistic approximation by using the non-relativistic kernel K_L^{NR} from Eq. (7) in the TPE sum rule. At leading order in $\not\pi$EFT expansion, we obtain

$$[\delta^A_{\mathrm{pol},L}]_{\mathrm{LO}} = -0.962\,\mathrm{meV}\,. \tag{47}$$

The NLO correction to $\delta^A_{\mathrm{pol},L}$ consists of two parts, whose sum gives

$$\Delta[\delta^A_{\mathrm{pol},L}]_{\mathrm{NLO}} = (-0.393 + 0.009)\,\mathrm{meV}\ . \tag{48}$$

The dominant contribution arising from $\rho_d\gamma$ expansion in the $\mathcal{Z}_d$ factor corresponding to the first term in Eq. (48) is given by $\rho_d\gamma[\delta^A_{\mathrm{pol},L}]_{\mathrm{LO}}$, and the rest is due to the NLO diagrams in Fig. 4. The dominant contribution to the NNLO correction on $\delta^A_{\mathrm{pol},L}$ arises from the $\rho_d\gamma$ expansion in $\mathcal{Z}_d$, and is given by $\rho_d\gamma\Delta[\delta^A_{\mathrm{pol},L}]_{\mathrm{NLO}}$. The NNLO diagrams in Fig. 5 lead to a contribution that is signicantly smaller. The sum of the two NNLO contributions yields

$$\Delta[\delta^A_{\mathrm{pol},L}]_{\mathrm{NNLO}} = (-0.157 + 0.004)\,\mathrm{meV}\ . \tag{49}$$

By summing up the contributions at each order, we obtain $\delta^A_{\text{pol},L}$ to be -0.962 meV, -1.346 meV and -1.499 meV at LO, NLO and NNLO respectively.

The $(\rho_d\gamma)$-expansion of $\mathcal{Z}_d$ clearly dominates the effective range corrections to $\delta^A_{\text{pol},L}$ and effects of diagrams that include final state interactions beyond NNLO are suppressed. The accuracy of the calculation can therefore be improved above NNLO by simply using the resummed wave function renormalization $\mathcal{Z}_d$ in the evaluation[2]. We first separate out the diagrammatic contributions at LO, NLO and NNLO respectively by setting $\mathcal{Z}_d$ equaling to its LO value $8\pi\gamma/m_N^2$. The sum of the results are then multiplied with an additional factor $1/(1-\rho_d\gamma)$ to match to the full wave function renormalization. By doing so, we have

$$\delta^A_{\text{pol},L} = \frac{1}{1-\rho_d\gamma}\,(-0.962+0.009+0.004)\ \text{meV} \ = -1.605\ \text{meV} \pm 0.066\ \text{meV}\ . \tag{50}$$

$\mathcal{Z}_d$-improvement can also be applied to the evaluation of the structure function, the result of which is shown in Fig. 6. The uncertainty presented in Eq. (50) is $\sim(\rho_d\gamma)^3$, where new $\not\pi$EFT parameters at higher orders are expected to enter.

In Table I, we show the $\not\pi$EFT results of $\delta^A_{\text{pol},L}$ computed at LO, NLO, NNLO and with the NNLO $\mathcal{Z}_d$-improvement approach. We also shown the comparison with Ref. [20] in the table, where the calculations were done using two different expansion methods, named η-less method and η-expansion method respectively. Using the η-less method, Ref. [20] evaluated $\delta^A_{\text{pol},L}$ in the multipole expansion of the charge operator and summing up multipole contributions to high orders. In the η-expansion approach, $\delta^A_{\text{pol},L}$ in the same non-relativistic and point-proton limit is equivalent to $\delta^A_{\text{pol},L} = \delta^{(0)}_{D1} + \delta^{(1)}_{Z3} + \delta^{(2)}_{R2} + \delta^{(2)}_{Q} + \delta^{(2)}_{D1D3}$ with notations given in Ref. [27]. Using nuclear potentials in the ZRA, η-less and η-expansion methods both obtained $\delta^A_{\text{pol},L} = -1.590$ meV [20], which is different by 0.8% from this work. Both $\not\pi$EFT and ZRA are based on the effective range expansion. However, in ZRA, only the bound-state wave function renormalization is range corrected as in $\mathcal{Z}_d$. In the work by Hernandez *et al.*, the intermediate scattering states in the two-photon processes were treated as plane waves subtracted by the bound ground state when using the ZRA potential. Using χEFT potential, where final-state interactions are embedded in the diagonalization of the nuclear Hamiltonian, $\delta^A_{\text{pol},L}$ obtained in η-less and η-expansion methods are respectively -1.588 and -1.590 meV [20]. The results from $\not\pi$EFT agree with both ZRA and χEFT calculations within the expected uncertainty at NNLO.

[2] Note that this is not Z-matching as introduced in Ref. [35] since we do not change the low-energy coefficients used in the evaluation of the transition matrix element.

The energy shift can be similarly evaluated in the relativistic limit by using the relativistic kernel from Eq. (6) in the sum rule integration. To obtain the η-expansion results of the relativistic $\delta^A_{\mathrm{pol},L}$ in ZRA (or χEFT), we need to add an additional relativistic correction 0.037 meV from Ref. [21] (or 0.030 meV from Ref. [27]) to the non-relativistic value. The resulting $\delta^A_{\mathrm{pol},L}$ is -1.553 meV in ZRA and -1.560 meV in χEFT. The relativistic $\delta^A_{\mathrm{pol},L}$ calculated using η-less method (noted by Δ_L in Ref. [20]) is -1.562 meV in χEFT. We calculate the relativistic η-less $\delta^A_{\mathrm{pol},L}$ in ZRA by using the analytic matrix element from Ref. [20] and obtain -1.564 meV. Results with $\not\pi$EFT in relativistic limit and comparison are also shown in Table I. It indicates that agreement within a 1% discrepancy in $\delta^A_{\mathrm{pol},L}$ is also achieved in the relativistic limit.

VI. SUMMARY

In this work, we have calculated the longitudinal structure function to NNLO in $\not\pi$EFT. We have given analytic expressions for the squared matrix element required to calculate the structure function. At NNLO, only two parameters, *i.e.*, the deuteron binding momentum and S-wave spin-triplet effective range, are required as experimental input. We furthermore included final and initial state interactions consistently and showed explicitly that final state interactions are strongly suppressed at higher orders. We separated out the dipole contribution to quantify how much S-wave final state interactions contribute to this process. The $\not\pi$EFT approach brings the advantage that calculations can be done largely analytical in the two-nucleon sector, and very few parameters are directly related to two-nucleon scattering enter the calculation. At NNLO, we expect for an accuracy of approximately 5%.

We compared our results for the energy shift $\delta^A_{\mathrm{pol},L}$ in μ-d with recent calculations using χEFT and ZRA nuclear potentials. We found good agreement with these calculations and confirm thereby our uncertainty estimate. We limited ourselves to NNLO because the deuteron channel shape parameter, two-body current counterterm and S-D mixing operator must be included at higher orders, making the analysis significantly more complicated. However, while much more involved, such a higher order calculation might also lead to interesting results, specifically if the unknown counterterm could be used to describe universal correlations between electromagnetic observables such as the deuteron radius and the nuclear polarizability correction.

Another extension of this work is to calculate the TPE contribution to the Lamb shift in the triton and Helium-3. Recent calculations show that the $\not\pi$EFT is well-suited to describe the electromagnetic properties of the three-nucleon system [36, 37]. In the three-nucleon system, $\not\pi$EFT loses some of its advantages. For example, the wave function has to be calculated numerically, too. We also expect significantly slower convergence and therefore larger uncertainties as the binding momentum of the three-nucleon states is much larger than the one of the deuteron. However, it is an important and interesting question by itself how well such details of the three-nucleon state can be described in $\not\pi$EFT.

ACKNOWLEDGMENTS

We thank Richard Hill for discussions in the early stages of this project and Sonia Bacca for comments on this manuscript. This work has been funded by the National Science Foundation under Grant No. PHY-1555030, by the Office of Nuclear Physics, U.S. Department of Energy under Contract No. DE-AC05-00OR22725 and by the National Natural Science Foundation of China under Grant No. 11805078.

Appendix A: Relevant loop integrals in the power-divergence subtraction scheme

1. Two-point loop integrals

We define the two-point loop integrals that are required in the calculation up through NNLO as in Ref. [34], such that

$$\begin{aligned}\mathcal{I}_{2n}^{\rm PDS}(E) &= i\int\frac{\mathrm{d}^4q}{(2\pi)^4}q^{2n}S(q_0+E,\boldsymbol{q})S(-q_0,-\boldsymbol{q})\\ &= -\frac{m_N}{4\pi}p^{2n}\left(\mu+ip\right)\ ,\end{aligned}\tag{A1}$$

where $p=\sqrt{m_N E}$ is the relative momentum within the two nucleon pair. For deuteron bound state we have $p=i\gamma$, with $\gamma=\sqrt{m_N B_d}$ denoting the deuteron binding momentum.

2. Loop integral $\mathcal{J}_0$

In diagram (c) of Fig. 3, the three-point loop integral $\mathcal{J}_0$ needed in Eq. (27) is given as

$$\mathcal{J}_{2n} = \int \frac{\mathrm{d}^4 l}{(2\pi)^4} l^{2n} iS(-B_d + l_0, \boldsymbol{l}) iS(-B_d + l_0 + \omega, \boldsymbol{l} + \mathbf{q}) iS(-l_0, \boldsymbol{l}) \ , \tag{A2}$$

which has three nucleon propagators in the integrand. This integral can be solved in various ways. One way that relates it to the calculation of a quantum mechanical matrix element of the charge operator is to solve it in coordinate space. We can reexpress the diagram as an integral over to coordinate space wave functions using Fourier transform of the two propagators

$$\begin{aligned} \frac{1}{-B_d - \frac{k^2}{m_N} + i\epsilon} &= -m_N \int \mathrm{d}^3 r e^{i\boldsymbol{k}\cdot\boldsymbol{r}} \frac{e^{-\gamma r}}{4\pi r} \ , \\ \frac{1}{E - \frac{(\boldsymbol{k}+\boldsymbol{q}/2)^2}{m_N} + i\epsilon} &= -m_N \int \mathrm{d}^3 r e^{i(\boldsymbol{k}+\boldsymbol{q}/2)\cdot\boldsymbol{r}} \frac{e^{ipr}}{4\pi r} \ , \end{aligned} \tag{A3}$$

where $E = p^2/m_N = \omega - B_d - q^2/(4m_N)$. For $\mathcal{J}_0$, placing the results of Eq. (A3) in Eq. (A2) gives

$$\mathcal{J}_0 = -8\pi \left(\frac{m_N}{4\pi}\right)^2 \int \mathrm{d}r e^{-\gamma r} e^{ipr} \frac{\sin(qr/2)}{qr} \ . \tag{A4}$$

Evaluating the integral in Eq. (A4), we find

$$\mathcal{J}_0 = -\frac{m_N^2}{4\pi q} \left[\cot^{-1}\left(\frac{m_N\omega - q^2/2}{q\gamma}\right) + i \tanh^{-1}\left(\frac{q\sqrt{m_N\omega - \gamma^2 - q^2/4}}{m_N\omega}\right) \right] \ , \tag{A5}$$

where we define the range of $\cot^{-1}$ as $(0, \pi)$.

In the evaluation of the matrix elements in this work we encounter the sum $\mathcal{J}_2 + \gamma^2 \mathcal{J}_0$. We can express this sum as

$$\mathcal{J}_2 + \gamma^2 \mathcal{J}_0 = m_N^2 \int \frac{\mathrm{d}^3 k}{(2\pi)^3} \frac{1}{m_N\omega - \gamma^2 - q^2/4 - k^2 + i\epsilon} \ . \tag{A6}$$

This integral can be solved using the PDS formula from KSW

$$\left(\mathcal{J}_2 + \gamma^2 \mathcal{J}_0\right)_{\mathrm{PDS}} = -\frac{m_N^2}{4\pi} \left(\mu + i\sqrt{m_N\omega - \gamma^2 - \frac{q^2}{4}}\right) = m_N \mathcal{I}_0(E) \ , \tag{A7}$$

with $m_N E = m_N\omega - \gamma^2 - q^2/4 = p^2$ due to energy conservation.

3. Loop integral $\widetilde{\mathcal{J}}_2$

At NLO, we encounter the loop diagram $\widetilde{\mathcal{J}}_2$ in the loop that has NLO final state interactions. We define it as

$$\tilde{\mathcal{J}}_2 = \int \frac{\mathrm{d}^4k}{(2\pi)^4}(\mathbf{k}+\frac{\boldsymbol{q}}{2})^2 iS(-B_d+k_0,\boldsymbol{k})iS(-B_d+k_0+\omega,\boldsymbol{k}+\boldsymbol{q})iS(-k_0,-\boldsymbol{k}) \ . \tag{A8}$$

Carrying out the countour integration gives

$$\tilde{\mathcal{J}}_2 = \int \frac{\mathrm{d}^3k}{(2\pi)^3}(\mathbf{k}+\frac{\boldsymbol{q}}{2})^2 i\left[-B_d-\frac{k^2}{m_N}+i\epsilon\right]^{-1} i\left[-B_d+\omega-\frac{q^2}{4m_N}-\frac{1}{m_N}(\boldsymbol{k}+\frac{\boldsymbol{q}}{2})^2+i\epsilon\right]^{-1} . \tag{A9}$$

We can now evaluate the relevant sum that involves $\widetilde{\mathcal{J}}_2$

$$\begin{aligned}\tilde{\mathcal{J}}_2 - p^2\mathcal{J}_0 &= \int \frac{\mathrm{d}^3k}{(2\pi)^3}\left[(\mathbf{k}+\frac{\boldsymbol{q}}{2})^2-\frac{p^2}{2}\right] i\left[-B_d-\frac{k^2}{m_N}+i\epsilon\right]^{-1} \\ &\qquad \times i\left[-B_d+\omega-\frac{q^2}{4m_N}-\frac{1}{m_N}(\boldsymbol{k}+\frac{\boldsymbol{q}}{2})^2+i\epsilon\right]^{-1} \\ &= \frac{m_N^2}{4\pi}(\gamma-\mu) \ ,\end{aligned} \tag{A10}$$

where we used $p^2 = m_N(\omega - B_d) - q^2/4$ to rewrite the denominator in the last factor in the integrand of Eq. (A10). Similarly, one can show that

$$\tilde{\mathcal{J}}_2 + \gamma^2\mathcal{J}_0 = m_N\mathcal{I}_0(E) = -\frac{m_N^2}{4\pi}(\mu+ip) \ . \tag{A11}$$

---

[1] I. Sick, "Precise radii of light nuclei from electron scattering," in Precision Physics of Simple Atoms and Molecules (Springer Berlin Heidelberg, Berlin, Heidelberg, 2008) pp. 57–77.

[2] R. Pohl et al., Metrologia **54**, L1 (2017).

[3] R. Pohl et al., Science **353**, 669 (2016).

[4] R. Pohl, Nature **466**, 213 (2010).

[5] A. Antognini, Science **339**, 417 (2013).

[6] P. J. Mohr, D. B. Newell, and B. N. Taylor, Rev. Mod. Phys. **88**, 035009 (2016).

[7] A. Beyer et al., Science **358**, 79 (2017).

[8] N. Bezginov, T. Valdez, M. Horbatsch, A. Marsman, A. Vutha, and E. Hessels, Science **365**, 1007 (2019).

[9] H. Fleurbaey, S. Galtier, S. Thomas, M. Bonnaud, L. Julien, F. Biraben, F. Nez, M. Abgrall, and J. Guna, Phys. Rev. Lett. **120**, 183001 (2018), arXiv:1801.08816 [physics.atom-ph].

[10] W. Xiong et al., Nature **575**, 147 (2019).

[11] E. Borie, Annals of Physics **327**, 733 (2012).

[12] K. Pachucki, D. Leibfried, and T. W. Hänsch, Phys. Rev. A **48**, R1 (1993).

[13] R. Rosenfelder, Nucl. Phys. A **393**, 301 (1983).

[14] Y. Lu and R. Rosenfelder, Physics Letters B **319**, 7 (1993).

[15] W. Leidemann and R. Rosenfelder, Phys. Rev. C **51**, 427 (1995).

[16] K. Pachucki, Phys. Rev. Lett. **106**, 193007 (2011).

[17] K. Pachucki and A. Wienczek, Phys. Rev. A **91**, 040503 (2015).

[18] O. Hernandez, C. Ji, S. Bacca, N. Nevo-Dinur, and N. Barnea, Physics Letters B **736**, 344 (2014).

[19] O. Hernandez, A. Ekstrm, N. Nevo-Dinur, C. Ji, S. Bacca, and N. Barnea, Phys. Lett. B **778**, 377 (2018).

[20] O. J. Hernandez, C. Ji, S. Bacca, and N. Barnea, Phys. Rev. C **100**, 064315 (2019), arXiv:1909.05717 [nucl-th].

[21] J. L. Friar, Phys. Rev. C **88**, 034003 (2013).

[22] C. E. Carlson, M. Gorchtein, and M. Vanderhaeghen, Phys. Rev. A **89**, 022504 (2014).

[23] J. L. Friar, Phys. Rev. C **16**, 1540 (1977).

[24] C. Ji, N. Nevo-Dinur, S. Bacca, and N. Barnea, Phys. Rev. Lett. **111**, 143402 (2013).

[25] N. Nevo-Dinur, C. Ji, S. Bacca, and N. Barnea, Physics Letters B **755**, 380 (2016).

[26] C. E. Carlson, M. Gorchtein, and M. Vanderhaeghen, Phys. Rev. A **95**, 012506 (2017).

[27] C. Ji, S. Bacca, N. Barnea, O. J. Hernandez, and N. Nevo-Dinur, J. Phys. G **45**, 093002 (2018), arXiv:1806.03101 [nucl-th].

[28] H.-W. Hammer, S. König, and U. van Kolck, Rev. Mod. Phys. **92**, 025004 (2020), arXiv:1906.12122 [nucl-th].

[29] H.-W. Hammer and L. Platter, Annu. Rev. Nucl. Part. Sci. **60**, 207 (2010).

[30] J. L. Friar, Annals of Physics **122**, 151 (1979).

[31] I. Sick, Phys. Rev. C **90**, 064002 (2014).

[32] N. Nevo-Dinur, O. J. Hernandez, S. Bacca, N. Barnea, C. Ji, S. Pastore, M. Piarulli, and R. B. Wiringa, Phys. Rev. C **99**, 034004 (2019).

[33] J.-W. Chen, G. Rupak, and M. J. Savage, Nucl. Phys. **A653**, 386 (1999), arXiv:nucl-th/9902056 [nucl-th].

[34] D. B. Kaplan, M. J. Savage, and M. B. Wise, Phys. Lett. **B424**, 390 (1998), arXiv:nucl-th/9801034.

[35] D. R. Phillips, G. Rupak, and M. J. Savage, Phys. Lett. **B473**, 209 (2000), arXiv:nucl-th/9908054.

[36] J. Vanasse, Phys. Rev. C **95**, 024002 (2017), arXiv:1512.03805 [nucl-th].

[37] J. Vanasse, Phys. Rev. C **98**, 034003 (2018), arXiv:1706.02665 [nucl-th].